

Ultra-broadband acoustic ventilation barrier based on multi-cavity resonators

Yu-Wei Xu(许雨薇), Yi-Jun Guan(管义钧), Cheng-Hao Wu(吴成昊), Yong Ge(葛勇), Qiao-Rui Si(司乔瑞), Shou-Qi Yuan(袁寿其), and Hong-Xiang Sun(孙宏祥)
Citation: Chin. Phys. B, 2023, 32 (**12**): 124303. DOI: 10.1088/1674-1056/acf5d1
Journal homepage: http://cpb.iphy.ac.cn; http://iopscience.iop.org/cpb

What follows is a list of articles you may be interested in

Nonlinear wave propagation in acoustic metamaterials with bilinear nonlinearity

Shiqi Liang(梁诗琪), Jiehui Liu(刘杰惠), Yun Lai(赖耘), and Xiaozhou Liu(刘晓宙)
Chin. Phys. B, 2023, 32 (**4**): 044301. DOI: 10.1088/1674-1056/ac9783

Controlling acoustic orbital angular momentum with artificial structures: From physics to application

Wei Wang(王未), Jingjing Liu(刘京京), Bin Liang (梁彬), and Jianchun Cheng(程建春)
Chin. Phys. B, 2022, 31 (**9**): 094302. DOI: 10.1088/1674-1056/ac7868

High-efficiency unidirectional wavefront manipulation for broadband airborne sound with a planar device

Yang Tan(谭杨), Bin Liang(梁彬), and Jianchun Cheng(程建春)
Chin. Phys. B, 2022, 31 (**3**): 034303. DOI: 10.1088/1674-1056/ac1e14

Tunable band gaps in acoustic metamaterials with periodic arrays of resonant shunted piezos

Chen Sheng-Bing (陈圣兵), Wen Ji-Hong (温激鸿), Wang Gang (王刚), Wen Xi-Sen (温熙森)
Chin. Phys. B, 2013, 22 (**7**): 074301. DOI: 10.1088/1674-1056/22/7/074301

Acoustic scattering from a submerged cylindrical shell coated with locally resonant acoustic metamaterials

Li Li (李黎), Wen Ji-Hong (温激鸿), Cai Li (蔡力), Zhao Hong-Gang (赵宏刚), Wen Xi-Sen (温熙森)
Chin. Phys. B, 2013, 22 (**1**): 014301. DOI: 10.1088/1674-1056/22/1/014301

Ultra-broadband acoustic ventilation barrier based on multi-cavity resonators

Yu-Wei Xu(许雨薇)[1], Yi-Jun Guan(管义钧)[1,2,†], Cheng-Hao Wu(吴成昊)[1], Yong Ge(葛勇)[1], Qiao-Rui Si(司乔瑞)[1], Shou-Qi Yuan(袁寿其)[1,‡], and Hong-Xiang Sun(孙宏祥)[1,2,§]

[1] *Research Center of Fluid Machinery Engineering and Technology, School of Physics and Electronic Engineering, Jiangsu University, Zhenjiang* 212013, *China*

[2] *State Key Laboratory of Acoustics, Institute of Acoustics, Chinese Academy of Sciences, Beijing* 100190, *China*

(Received 2 June 2023; revised manuscript received 27 July 2023; accepted manuscript online 1 September 2023)

The numerical simulations and experimental results of an ultra-broadband acoustic ventilation barrier composed of periodic unit cells are reported in this paper. Based on multiple mechanisms, including sound absorption by eigenmodes of the unit cell and sound reflection by a plate structure on upper surface of the unit cell, a single-layer ventilation barrier with broadband sound reduction is designed, and its working bandwidth can reach about 1560 Hz. The experimental results accord well with the simulation results. Furthermore, two types of three-layer ventilation barriers are designed and demonstrated by using the unit cells with different values of a (the length of the hollow square region) and w (the width of the channel between the adjacent cavities), and the bandwidths of both ventilation barriers can increase to 3160 Hz and 3230 Hz, respectively. The designed barrier structures have the advantages of ultra-broadband sound reduction and ventilation, which paves the way to designing high-performance ventilation barriers for the applications in environmental protection and architectural acoustics.

Keywords: acoustic metamaterials, ultra-broadband sound reduction, acoustic barrier, ventilation

PACS: 43.35.+d, 43.20.+g **DOI:** 10.1088/1674-1056/acf5d1

1. Introduction

Sound reduction has always attracted a great deal of attention due to its practical applications in the fields of noise control, environmental protection and architectural acoustics. Recent development of acoustic metamaterials[1–9] and metasurfaces[10–17] provides alternative methods for designing various sound insulation and sound absorption systems based on different types of unit cells, such as Helmholtz resonators,[18–24] coiled Fabry–Perot resonators,[25–27] sound membranes,[28–31] metasurface-based structures,[32–40] and split-ring-resonators.[41,42] Generally, these systems have the advantages of high-performance sound insulation and absorption. However, most of them are designed as closed structures, and it is difficult to use them in the application scenarios requiring an additional feature of ventilation.

To overcome it, a variety of ventilation structures with sound insulation and absorption based on different mechanisms have been realized sequentially,[43–48] which mainly include sound absorber based on weak coupling of two identical oppositely oriented split tube resonators,[43] open sound silencer based on Fano-like interference,[45–47] and ultra-sparse open sound-insulation wall based on artificial Mie resonances.[48] Beyond that, ultrathin metasurface-based structures[49] have been proposed to design ventilated sound insulation systems based on phased modulation, such as acoustic metacages,[50] open tunnels,[51] and windows.[52] These types of structures can realize sound insulation/absorption and ventilation simultaneously, however, the working bandwidths are narrow owing to resonance nature. In order to solve this problem, several researches[53–59] have been devoted to optimizing working bandwidths of sound insulation/sound absorption, such as ultra-wideband ventilation barrier[53] based on sound dissipation mechanism and interference mechanism, and ventilated sound metamaterial and sound absorption metamaterial based on the coupling modulation of resonance energy leakage and loss.[59] However, it still poses a great challenge to further increasing the bandwidth of ventilated sound-reduction structures.

In this work, we propose an ultra-broadband acoustic ventilation barrier composed of periodic unit cells. The designed single-layer ventilation barrier can realize broadband sound reduction with a bandwidth of 1560 Hz. Such a phenomenon arises from sound absorption caused by the eigenmode of the unit cell and sound reflection by the plate structure on upper surface of the unit cell. The measured and simulated results accord well with each other. Moreover, by designing two types of three-layer ventilation barriers composed of the unit cells with different values of a (the length of the hollow square region) and w (the width of the channel between the adjacent

†Corresponding author. E-mail: gyjlxy@ujs.edu.cn
‡Corresponding author. E-mail: Shouqiy@ujs.edu.cn
§Corresponding author. E-mail: jsdxshx@ujs.edu.cn

© 2023 Chinese Physical Society and IOP Publishing Ltd

cavities), we can increase the working bandwidths of both barriers to 3160 Hz and 3230 Hz, respectively, which are demonstrated by the experimental measurement.

2. Design of acoustic ventilation barrier

As shown in Fig. 1(a), we designed a type of acoustic ventilation barrier composed of periodic unit cells with a thickness of H. The photographs of the upper surface, bottom surface, and cross section of the unit cell made of epoxy resin are shown in Figs. 1(b)–1(d), respectively. We can see that there exists a hollow square region in the middle of the unit cell, realizing a characteristic of ventilation. Additionally, as shown in Fig. 1(d), the unit cell is composed of a multiple-cavity resonator and different plate structures on both sides, in which the multiple-cavity resonator consists of four interconnected identical cavities surrounded by four channels. The parameters D, w, t, a, b, and c are the length of the unit cell, the width of the channel between the adjacent cavities, the thickness of the wall, the length of the hollow square region, the open width of the cavities, and the width of the channel between the cavities and outer frame, respectively [as shown in Fig. 1(e)]. The performance of the ventilation barrier is numerically simulated by the software of COMSOL Multiphysics. Owing to sound absorption caused by thermoviscous energy loss, the module of thermoviscous acoustic-solid interaction was used inside the unit cell, while the module of acoustic pressure was adopted in other parts to reduce computation cost. Here, it is noted that the surfaces inside the unit cell were set as the thermoviscous boundary layers, and the thickness of the layer is $d_{\mathrm{v}} = \sqrt{2\mu/(\rho\omega)}$, in which the parameters μ, ρ, and ω are the coefficient of dynamic viscosity, the density of air, and the angular frequency, respectively. In the numerical model, the parameters H, D, w, t, a, b, and c are selected as 3.0 cm, 10.0 cm, 1.0 cm, 1.5 mm, 4.0 cm, 4.0 mm, and 4.0 mm, respectively. The parameters of epoxy resin used in the simulation are the density $\rho = 1180$ kg/m^3, the longitudinal wave velocity $c_{\mathrm{l}} = 2720$ m/s, and the transversal wave velocity $c_{\mathrm{t}} = 1460$ m/s, and those of air are calculated from $\rho = p_0 M/(RT)$ and $c = \sqrt{\gamma RT/M}$, in which the ratio of the molar heat capacities γ, the molar mass M, the air temperature T, the molar gas constant R, and the air pressure p_0 are selected as 1.4, 28.97×10^{-3} kg/mol, 293 K, 8.31 J/(mol/K), and 101.325 kPa, respectively.

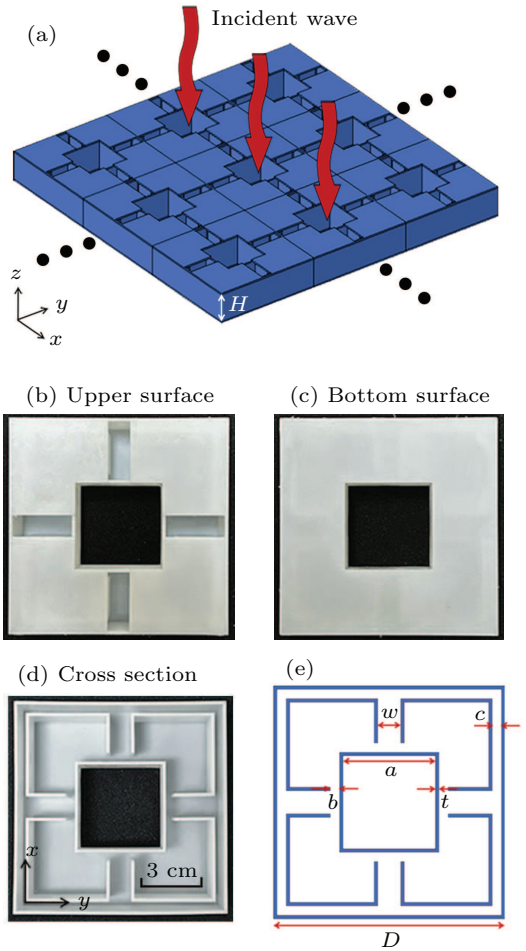


Fig. 1. (a) Schematic diagram of acoustic ventilation barrier composed of periodically arranged unit cells. Photograph of (b) upper surface, (c) bottom surface, and (d) cross section of the unit cell, (e) schematic diagram of cross section of the unit cell.

3. Performance and mechanism of acoustic ventilation barrier

To demonstrate the performance of the designed ventilation barrier, we conducted an experiment to measure transmittance spectra of a unit cell in a straight waveguide made of acrylic plates with a size of 2 m×0.1 m×0.1 m [as shown in Fig. 2(a)], in which the sound-absorbing foams are placed on both sides of the waveguide to eliminate reflected sound energy. The sample is placed in the middle of the waveguide, and the width of the waveguide is the same as the length of the unit cell. Beyond that, a loudspeaker driven by a power amplifier is placed on the left side to generate incident sound signals. Four 0.25-inch (1 inch = 2.54 cm) microphones (Brüel & Kjær type-4954, marked as Mic. 1, 2, 3, and 4) are inserted into the waveguide from four holes with the same size to detect sound signals. The measured data are recorded by the module of Brüel & Kjær 3160-A-042, and they are analyzed by the software of PULSE Labshop.

The acoustic pressure on the left of the sample in the waveguide is the superposition of the incident sound signal and reflected sound signal, and that on the right of the sample is the superposition of the transmitted sound signal and reflected sound signal. Thus, the sound pressures at the positions 1, 2, 3, and 4 can be expressed as

$$p_1 = p_{\mathrm{i}}\,\mathrm{e}^{\mathrm{i}k(d_1+l_1)} + p_{\mathrm{r}}\,\mathrm{e}^{-\mathrm{i}k(d_1+l_1)}, \tag{1}$$

$$p_2 = p_i e^{ikl_1} + p_r e^{-ikl_1}, \tag{2}$$

$$p_3 = p_t e^{-ikl_2} + p_{tr} e^{ikl_2}, \tag{3}$$

$$p_4 = p_t e^{-ik(d_2+l_2)} + p_{tr} e^{ik(d_2+l_2)}, \tag{4}$$

where k is the wave number of air, and p_i and p_t are the incident acoustic pressure and transmitted acoustic pressure, respectively, and p_r and p_{tr} are the reflected sound pressure in the left region and that in the right region of the waveguide, respectively, and d_1 and d_2 are the distance between Mic. 1 and Mic. 2, and that between Mic. 3 and Mic. 4, respectively, and l_1 and l_2 are the distance from Mic. 2 to the left surface and that from Mic. 3 to the right surface of the sample, respectively. Here, we select $d_1 = d_2 = 10$ cm, and $l_1 = l_2 = 13.5$ cm. According to Eqs. (1) and (2), we can obtain

$$p_i = \frac{p_1 e^{-ikl_1} - p_2 e^{-ik(d_1+l_1)}}{e^{ikd_1} - e^{-ikd_1}}, \tag{5}$$

$$p_r = \frac{p_2 e^{ik(d_1+l_1)} - p_1 e^{ikl_1}}{e^{ikd_1} - e^{-ikd_1}}. \tag{6}$$

Thus, the reflection coefficient can be given as

$$R = \frac{p_r}{p_i} = \frac{p_2 e^{ikd_1} - p_1}{p_1 - p_2 e^{-ikd_1}} e^{2ikl_1}. \tag{7}$$

From Eqs. (3) and (4), we can obtain

$$p_t = \frac{p_3 e^{ik(d_2+l_2)} - p_4 e^{ikl_2}}{e^{ikd_2} - e^{-ikd_2}}. \tag{8}$$

Thus, the transmitted coefficient can be expressed as

$$T = \frac{p_t}{p_i} = \frac{\sin kd_1}{\sin kd_2} \frac{p_3 e^{ikd_2} - p_4}{p_1 - p_2 e^{-ikd_1}} e^{ik(l_1+l_2)}. \tag{9}$$

From Eqs. (7) and (9), we can calculate the transmittance, reflectance, and absorptance of the sample to be $t = |T|^2$, $r = |R|^2$, and $\alpha = 1 - |R|^2 - |T|^2$, respectively.

Figure 2(b) shows the measured transmittance spectra caused by the unit cell, in which the simulated results for the unit cell under the conditions of the hard and periodic boundary are also provided for comparisons. We can see that in the range of 834 Hz–2395 Hz (black shaded region), the transmittances are lower than 0.1, and thus the working bandwidth can reach about 1560 Hz, showing a typical characteristic of broadband sound reduction. Both types of simulated transmittance spectra are almost the same, and thus we can use the performance of a single unit cell to characterize that of the designed acoustic barrier. Beyond that, the measured and simulated results are basically in agreement with each other, in which the disagreement between both results may arise from the leakage of sound energy from the acrylic plates of the waveguide and the structural deviation of sample caused by the three-dimensional (3D) printing. Furthermore, according to the proportion of the size of the hollow region in the unit cell, we can obtain that the ventilation ratio of the designed barrier is 16%.

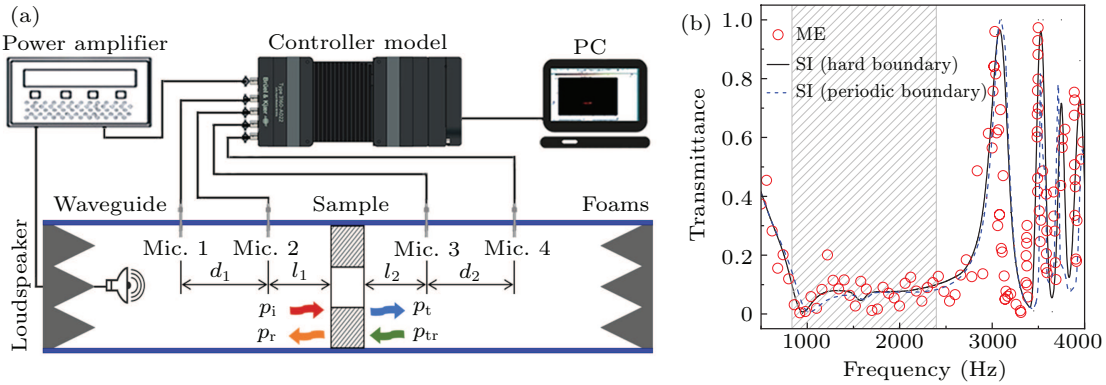


Fig. 2. (a) Experimental set-up. (b) Measured (ME) and simulated (SI) transmittance spectra caused by the unit cell, with solid black line and dashed blue lines denoting simulated results for the unit cell under numerical condition of hard boundary and periodic boundary, respectively.

To explore the mechanism of the ventilation barrier, we simulate the absorptance and reflectance spectra caused by the unit cell. As shown in Fig. 3(a), the broadband sound reduction is closely related to both sound absorption and reflection. To further explain it, we divide the working band into four regions (I: 834 Hz–1150 Hz, II: 1150 Hz–1450 Hz, III: 1450 Hz–1700 Hz, and IV: 1700 Hz–2395 Hz) according to different characteristics. In the bands I and III, the absorptance values are both larger than 0.1, and the transmittance values are both lower than 0.1, however, both absorptance value and transmittance value are lower than 0.1 in the bands II and IV. We can see that the band I is determined by both sound absorption and sound reflection simultaneously, and the bands II and IV are mainly caused by sound reflection, which arises from the plate structure on upper surface of each unit cell. However, in the band III, the absorption coefficients are larger than 0.1, and the maximum value can reach a value exceeding 0.9 at 1580 Hz, so the band III is attributed to sound absorption caused by the unit cell.

Next, to provide an insight into the mechanism of sound absorption in the bands I and III, we simulate the pressure amplitude eigenfunctions of the unit cell around two absorption

peaks in the bands I and III. As shown in Fig. 3(b), there exist two types of eigenmodes at 920 Hz and 1578 Hz, in which most of the sound energy is absorbed into four cavities at 920 Hz, and it is mainly concentrated into the channel between the cavities and the outer frame at 1578 Hz. Figure 3(c) shows the simulated pressure amplitude distributions in the unit cell excited by the normal incidence of sound at 920 Hz and 1580 Hz. We can see that the field distributions in the unit cell are consistent with those of two eigenmodes in Fig. 3(b), indicating that the sound absorption is closely related to the eigenmodes of the unit cell. Moreover, we simulate the distributions of thermoviscous energy loss density in the unit cell at 920 Hz and 1580 Hz. As shown in Fig. 3(d), the thermoviscous loss is mainly distributed in the narrow channel between the cavity and the outer frame at 1580 Hz, which is much stronger than that in the channels between the adjacent cavities at 920 Hz. Such a phenomenon can be used to explain the difference between the two absorption peaks in the bands I and III. Therefore, the absorbed sound energy is mainly dissipated by the thermoviscous loss inside the channels of the unit cell in the bands I and III.

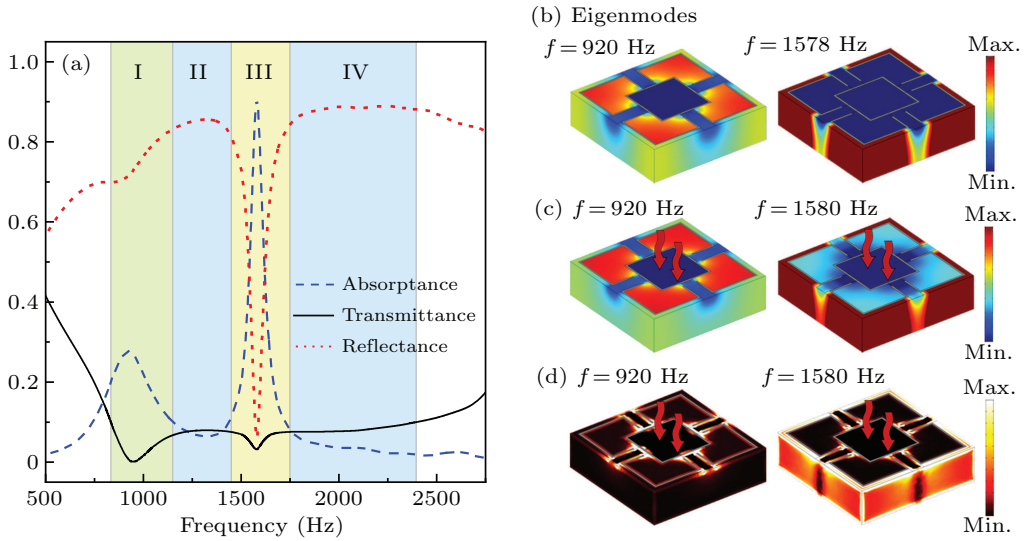


Fig. 3. (a) Simulated sound transmittance, reflectance, and absorptance spectra caused by the unit cell. Different colors represent four working bands (I: 834 Hz–1150 Hz, II: 1150 Hz–1450 Hz, III: 1450 Hz–1700 Hz, and IV: 1700–2395 Hz). (b) Simulated pressure amplitude eigenfunctions of the unit cell at 920 Hz and 1578 Hz. Simulated distributions of (c) pressure amplitude and (d) thermoviscous energy loss density in the unit cell excited by normal incidence of sound (red solid arrows) at 920 Hz and 1580 Hz.

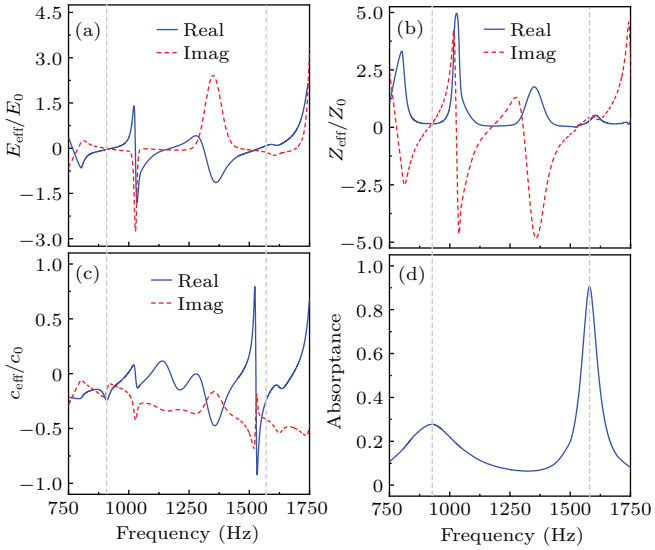


Fig. 4. Simulated (a) effective bulk modulus, (b) effective impedance, (c) effective sound velocity, and (d) absorptance spectra of the unit cell around two absorption peaks.

To further analyze the above phenomena, we also simulate the effective bulk modulus, the effective impedance, the effective sound velocity of the unit cell, which are presented in Figs. 4(a)–4(c), respectively, and the absorptance spectrum of the unit cell [as shown in Fig. 4(d)] is also exhibited for comparisons. We can see that the real part of the effective bulk modulus is close to zero at 920 Hz and 1578 Hz [as shown in Fig. 4(a)] owing to the excitation of the eigenmodes at both frequencies. Additionally, the imaginary part of the effective

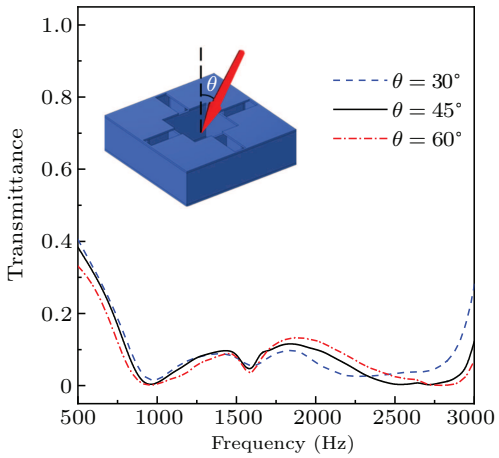


Fig. 5. Simulated transmittance spectra through unit cell under the excitation of acoustic waves at different incident angles.

impedance and sound velocity at 1578 Hz are larger than those at 920 Hz [as shown in Figs. 4(b) and 4(c)], indicating the high concentration and dissipation of sound energy in the unit cell at 1578 Hz.[39] The theoretical analysis of these effective parameters accords well with the characteristics of the unit cell in Fig. 3.

Figure 5 shows the simulated transmittance spectra through the unit cell under the excitation of the acoustic waves at the incident angle $\theta = 30°$, 45°, and 60°. We can see that the simulated transmittance spectra are almost the same at different incident angles of sound, indicating high-performance broadband sound insulation in a wide range of incident angle for the designed ventilation barrier.

4. Bandwidth optimization of acoustic ventilation barrier

To optimize the bandwidth of the designed ventilation barrier, we also study and measure the transmission characteristics caused by the unit cell with different values of a and w, which is shown in Fig. 6. We can observe that by adjusting the parameter a or w, the ventilation barrier has high-performance sound reduction below 3000 Hz, and the measured results are in good agreement with the numerical results.

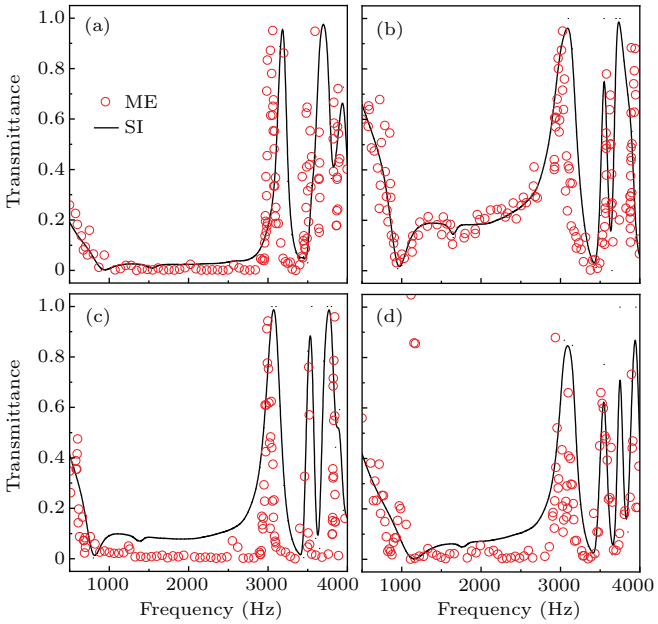


Fig. 6. Measured and simulated transmittance spectra caused by unit cell with (a) $a = 3$ cm, $w = 10$ mm; (b) $a = 5$ cm, $w = 10$ mm; (c) $a = 4$ cm, $w = 5$ mm; and (d) $a = 4$ cm, $w = 15$ mm.

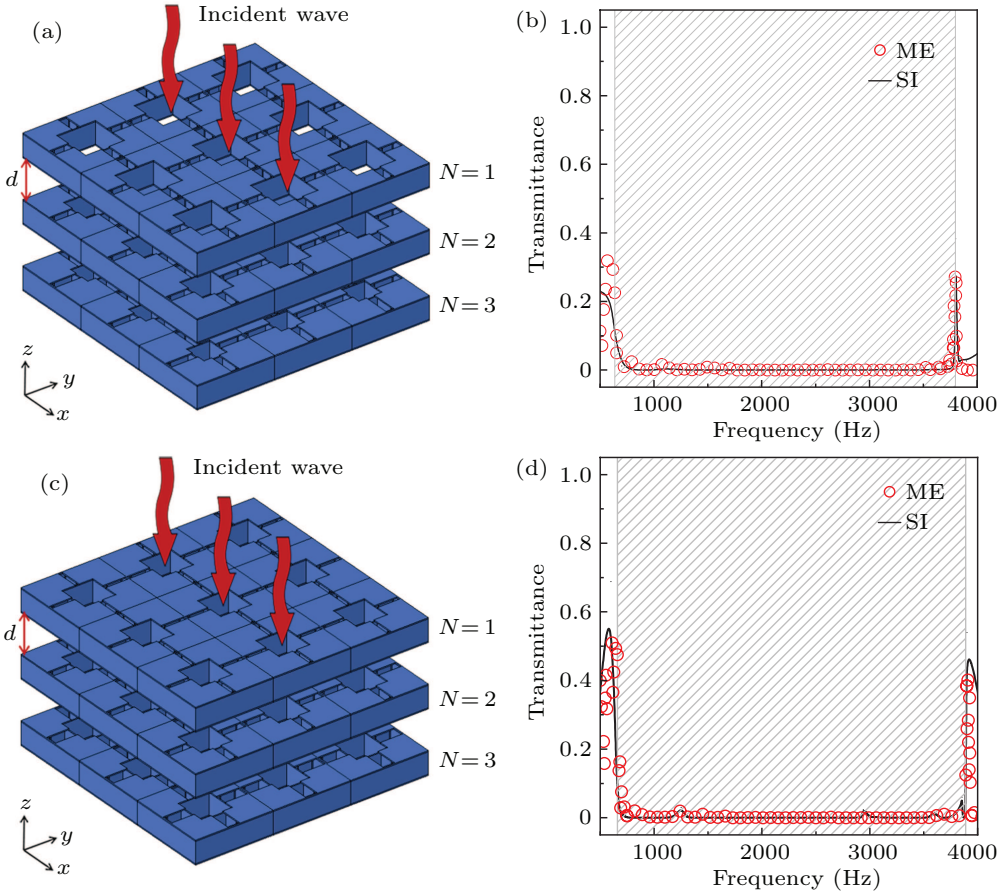


Fig. 7. (a) Schematic diagram of the first type of three-layer ventilation barrier composed of unit cells with the same value of w ($w = 10$ mm) but different values of a ($a = 5$ cm for $N = 1$; $a = 4$ cm for $N = 2$; $a = 3$ cm for $N = 3$). (b) Measured and simulated transmittance spectra caused by the three-layer ventilation barrier. (c) Schematic diagram of the second type of three-layer barrier composed of unit cells with the same value of a ($a = 4$ cm) but different values of w ($w = 5$ mm for $N = 1$; $w = 10$ mm for $N = 2$; $w = 15$ mm for $N = 3$). (d) Measured and simulated transmittance spectra caused by three-layer ventilation barrier.

Next, we design two types of three-layer ventilation barriers with different values of a and w to realize an ultra-broadband feature. Figure 7(a) schematically shows the first type of three-layer ventilation barrier with a distance (denoted as d) of 4.5 cm, in which the values of parameter a of the unit cells in layers 1, 2, and 3 are selected as 5 cm, 4 cm, and 3 cm, respectively, and the other parameters are the same as those in Fig. 1(e). Here, it is necessary to point out that the ventilation ratio of the three-layer barrier is 9% owing to different values of a, which decreases obviously in comparison with that of the single-layer barrier. Figure 6(b) shows the measured and simulated transmittance spectra of the three-layer ventilation barriers. We observed that the transmittance values are all less than 0.1 in the frequency range of 636 Hz–3798 Hz, and the bandwidth can reach about 3160 Hz, demonstrating the ultra-broadband characteristic. The measured and simulated results match well with each other.

Figure 7(c) presents the second type of three-layer ventilation barrier, in which the values of w of the unit cells in each layer ($N = 1$, 2, and 3) are selected as 5 mm, 10 mm, and 15 mm, respectively, and the distance between two adjacent layers is the same as that in Fig. 7(a). Here, the ventilation ratio of this type of three-layer barrier is 16%, which is consistent with that of the single-layer barrier. The measured and simulated transmittance spectra of the three-layer ventilation barrier are shown in Fig. 7(d). It is observed that the transmittance values are all below 0.1 in the frequency range of 660 Hz–3890 Hz (black shaded region), and the working bandwidth can increase to 3230 Hz, indicating the realization of an ultra-broadband characteristic of the ventilation barrier. The measured results show excellent agreement with the numerical results. Such ultra-broadband working bandwidths of both three-layer ventilation barriers are closely related to the bandgaps of the unit cells with different values of a and w (as shown in Fig. 6) and sound scattering and reflection between the adjacent barriers. Thus, we can effectively optimize the bandwidth of the designed ventilation barrier by using multi-layer systems.

5. Conclusions

In this work, we have designed and demonstrated an ultra-broadband acoustic ventilation barrier. By designing a single-layer ventilation barrier, we can observe a broadband sound reduction with the working bandwidth of 1560 Hz, which is attributed to the multiple mechanism, such as the sound absorption caused by the eigenmodes of the unit cell and the sound reflection by the plate structure on upper surface of the unit cell. Additionally, we study the sound-reduction performances of the unit cell by adjusting the parameters a and w. As a result, we design two types of three-layer ventilation barriers composed of the unit cells with different values of a and w, which can achieve the ultra-broadband characteristics with the working bandwidths of 3160 Hz and 3230 Hz, respectively. The performances of these ventilation barriers are verified by experimental measurements. The proposed ventilation barriers with ultra-broadband sound reduction have a great potential in environmental protection and architectural acoustics.

Acknowledgements

Project supported by the National Natural Science Foundation of China (Grant Nos. 12174159, 12274183, and 51976079), the National Key Research and Development Program of China (Grant No. 2020YFC1512403), and the Research Project of State Key Laboratory of Mechanical System and Vibration (Grant No. MSV202201).

References

[1] Fang N, Xi D J, Xu J Y, Ambati M, Srituravanich W, Sun C and Zhang X 2006 *Nat. Mater.* **5** 452
[2] Jia D, Wang Y, Ge Y, Yuan S Q and Sun H X 2021 *Prog. Electromagn. Res.* **172** 13
[3] Liang Z X and Li J S 2012 *Phys. Rev. Lett.* **108** 114301
[4] Cummer S A, Christensen J and Alù A 2016 *Nat. Rev. Mater.* **1** 16001
[5] Ma G C and Sheng P 2016 *Sci. Adv.* **2** e1501595
[6] Gao N S, Zhang Z C, Deng J, Guo X Y, Cheng B Z and Hou H 2022 *Adv. Mater. Technol.* **7** 2100698
[7] Tsang L, Liao T H and Tan S R 2021 *Prog. Electromagn. Res.* **171** 137
[8] Yu S Y, Ni X, Xu Y L, He C, Nayar P, Lu M H and Chen Y F 2016 *Chin. Phys. Lett.* **33** 044302
[9] Geng Z G, P Y G, Shen Y X, Zhao D G and Zhu X F 2019 *Acta Phys. Sin.* **68** 227802 (in Chinese)
[10] Li Y, Liang B, Gu Z M, Zou X Y and Cheng J C 2013 *Sci. Rep.* **3** 2546
[11] Mei J and Wu Y 2014 *New J. Phys.* **16** 123007
[12] Tang K, Qiu C Y, Ke M Z, Lu J Y, Ye Y T and Liu Z Y 2014 *Sci. Rep.* **4** 6517
[13] Yan Q H, Chen H S and Yang Y H 2021 *Prog. Electromagn. Res.* **172** 33
[14] Zhang H, Xiao Y, Wen J H, Yu D L and Wen X S 2016 *Appl. Phys. Lett.* **108** 141902
[15] Assouar B, Liang B, Wu Y, Li Y, Cheng J C and Jing Y 2018 *Nat. Rev. Mater.* **3** 460
[16] Quan L, Sounas D L and Alù A 2019 *Phys. Rev. Lett.* **123** 064301
[17] Hu Z P, He N, Sun Y W, Jin Y and He S L 2021 *Prog. Electromagn. Res.* **172** 51
[18] Romero-Garcia V, Theocharis G, Richoux O, Merkel A, Tournat V and Pagneux V 2016 *Sci. Rep.* **6** 19519
[19] Jimenez N, Huang W, Romero-Garcia V, Pagneux V and Groby J P 2016 *Appl. Phys. Lett.* **109** 121902
[20] Li J F, Wang W Q, Xie Y B, Popa B I and Cummer S A 2016 *Appl. Phys. Lett.* **109** 091908
[21] Jimenez N, Romero-Garcia V, Pagneux V and Groby J P 2017 *Phys. Rev. B* **95** 014205
[22] Long H Y, Cheng Y and Liu X J 2017 *Appl. Phys. Lett.* **111** 143502
[23] Huang S B, Zhou Z L, Li D T, Liu T, Wang X, Zhu J and Li Y 2020 *Sci. Bull.* **65** 373
[24] Li L J, Zheng B, Zhong L M, Yang J, Liang B and Cheng J C 2018 *Appl. Phys. Lett.* **113** 103501
[25] Zhang C and Hu X H 2016 *Phys. Rev. Appl.* **6** 064025
[26] Yang M, Chen S Y, Fuab C X and Sheng P 2017 *Mater. Horiz.* **4** 673
[27] Jimenez N, Romero-Garcia V, Pagneux V and Groby J P 2017 *Sci. Rep.* **7** 13595
[28] Mei J, Ma G C, Yang M, Yang Z Y, Wen W J and Sheng P 2012 *Nat. Commun.* **3** 756
[29] Ma G C, Yang M, Xiao S W, Yang Z Y and Sheng P 2014 *Nat. Mater.* **13** 873
[30] Yang M, Li Y, Meng C, Fu C X, Mei J, Yang Z Y and Sheng P 2015 *Comptes. Rendus. Méc.* **343** 635

[31] Yang M, Meng C, Fu C X, Li Y, Yang Z Y and Sheng P 2015 *Appl. Phys. Lett.* **107** 104104
[32] Cai X B, Guo Q Q, Hu G K and Yang J 2014 *Appl. Phys. Lett.* **105** 121901
[33] Li Y and Assouar B 2016 *Appl. Phys. Lett.* **108** 063502
[34] Tang Y F, Xin F X, Huang L X and Lu T J 2017 *Eur. Phys. Lett.* **118** 44002
[35] Chang H T, Liu L, Zhang C and Hu X H 2018 *AIP Adv.* **8** 045115
[36] Wang X L, Luo X D, Zhao H and Huang Z Y 2018 *Appl. Phys. Lett.* **112** 021901
[37] Donda K, Zhu Y F, Fan S W, Cao L Y, Li Y and Assouar B 2019 *Appl. Phys. Lett.* **115** 173506
[38] Long H Y, Shao C, Liu C, Cheng Y and Liu X J 2019 *Appl. Phys. Lett.* **115** 103503
[39] Shao C, Long H Y, Chen Y and Liu X J 2019 *Sci. Rep.* **9** 13482
[40] Donda K, Zhu Y F, Merkel A, Fan S W, Cao L Y, Wan S and Assouar B 2021 *Smart Mater. Struct.* **30** 085003
[41] Wu X X, Fu C X, Li X, Meng Y, Gao Y B, Tian J X, Wang, L, Huang Y Z, Yang Z Y and Wen W J 2016 *Appl. Phys. Lett.* **109** 043501
[42] Xu Z X, Meng H Y, Chen A, Yang J, Liang B and Cheng J C 2021 *J. Appl. Phys.* **129** 094502
[43] Wu X X, Au-Yeung K Y, Li X, Roberts R C, Tian J X, Hu C D, Huang Y Z, Wang S X, Yang Z Y and Wen W J 2018 *Appl. Phys. Lett.* **112** 103505
[44] Kumar S and Lee H P 2020 *Appl. Phys. Lett.* **116** 134103
[45] Ghaffarivardavagh R, Nikolajczyk J, Anderson S and Zhang X 2019 *Phys. Rev. B* **99** 024302
[46] Zhang H L, Zhu Y F, Liang B, Yang J and Cheng J C 2017 *Appl. Phys. Lett.* **111** 203502
[47] Xu Z X, Zheng B, Yang J, Liang B and Cheng J C 2021 *Phys. Rev. Appl.* **16** 044020
[48] Cheng Y, Zhou C, Yuan B G, Wu D J, Wei Q and Liu X J 2015 *Nat. Mater.* **14** 1013
[49] Yu N F, Genevet P, Kats M A, Aieta F, Tetienne J P, Capasso F and Gaburro Z 2011 *Science* **334** 333
[50] Shen C, Xie Y B, Li J F, Cummer S A and Jing Y 2018 *J. Appl. Phys.* **123** 124501
[51] Zhu Y F, Gu Z M, Liang B, Yang J, Yang J, Yin L L and Cheng J C 2016 *Appl. Phys. Lett.* **109** 103504
[52] Ge Y, Sun H X, Yuan S Q and Lai Y 2019 *Phys. Rev. Mater.* **3** 065203
[53] Dong R Z, Mao D X, Wang X and Li Y 2021 *Phys. Rev. Appl.* **15** 024044
[54] Xu Z X, Gao H, Ding Y J, Yang J, Liang B and Cheng J C 2020 *Phys. Rev. Appl.* **14** 054016
[55] Chen A, Xu Z X, Zheng B, Yang J, Liang B and Cheng J C 2022 *Appl. Phys. Lett.* **120** 033501
[56] Wang Z W, Chen A, Xu Z X, Yang J, Liang B and Cheng J C 2023 *Sci. China-Phys. Mech. Astron.* **66** 224311
[57] Liu C K, Wang H J, Liang B, Cheng J C and Lai Y 2022 *Appl. Phys. Lett.* **120** 231702
[58] Tang Y F, Liang B and Lin S Y 2022 *J. Acoust. Soc. Am.* **152** 2412
[59] Gao Y X, Li Z W, Liang B, Yang J and Cheng J C 2022 *Appl. Phys. Lett.* **120** 261701